Title
Structure of the posttranslational Sec protein-translocation channel complex from yeast

Journal
Science, 363(6422)

ISSN
0036-8075

Authors
Itskanov, Samuel
Park, Eunyong

Publication Date
2019-01-04

DOI
10.1126/science.aav6740

Peer reviewed

Structure of the posttranslational Sec protein-translocation channel complex from yeast

Samuel Itskanov[1] and Eunyong Park[2,#]

[1]Biophysics Graduate Program, University of California, Berkeley, Berkeley, CA 94720, USA.

[2]Department of Molecular and Cell Biology and California Institute for Quantitative Biosciences, University of California, Berkeley, Berkeley, CA 94720, USA.

[#]Corresponding author. Email: eunyong_park@berkeley.edu

ABSTRACT

The Sec61 protein-conducting channel mediates transport of many proteins, such as secretory proteins, across the endoplasmic reticulum (ER) membrane during or after translation. Posttranslational transport is enabled by two additional membrane proteins associated with the channel, Sec63 and Sec62, but its mechanism was poorly understood. Here we determined a structure of the Sec complex (Sec61-Sec63-Sec71-Sec72) from *Saccharomyces cerevisiae* by cryo-electron microscopy (cryo-EM). The structure shows that Sec63 tightly associates with Sec61 though interactions in cytosolic, transmembrane, and ER-luminal domains, prying open Sec61's lateral gate and translocation pore and thus activating the channel for substrate engagement. Furthermore, Sec63 optimally positions binding sites for cytosolic and luminal chaperones in the complex to enable efficient polypeptide translocation. Our study provides mechanistic insights into eukaryotic posttranslational protein translocation.

The eukaryotic Sec61 or prokaryotic SecY complex forms a universally conserved protein-conducting channel that is essential for biogenesis of many proteins (*1-3*). The channel mediates transport of soluble (e.g., secretory) proteins across the eukaryotic ER membrane or the prokaryotic plasma membrane through its water-filled pore and integration of membrane proteins into the lipid phase through its lateral gate. The Sec61/SecY channel consists of an hourglass-shaped α-subunit, which contains 10 transmembrane segments (TMs 1–10), and two small β- and γ-subunits, which are single-pass membrane proteins in eukaryotes (*4*). Often, translocation is coupled with translation (i.e., cotranslational translocation) by direct docking of a translating ribosome onto the channel. The channel also translocates many proteins in a posttranslational manner, the mechanisms of which differ between eukaryotes and prokaryotes. In eukaryotes, posttranslational translocation requires two essential membrane proteins Sec63 and Sec62, which associate with the channel (*5-8*), and the ER-resident Hsp70 chaperone BiP, which grasps the substrate polypeptide in the ER lumen and prevents it from backsliding to the cytosol (*9-12*). In fungal species, the complex (hereafter referred to as the Sec complex) is further associated with the nonessential Sec71 and Sec72 subunits (*10, 11, 13*). The molecular architecture of the Sec complex and the functions of its subunits are poorly defined.

To gain insight into Sec-mediated protein translocation, we determined a structure of the *Saccharomyces cerevisiae* Sec complex at 3.7-Å resolution by cryo-EM (Fig. 1, and figs S1 and S2). Many side chains are clearly visible in the density map, enabling modeling of an accurate atomic structure (Fig. 1B, and fig S2C). The map also allowed us to improve the model for the eukaryotic Sec61 channel, which was previously built into maps at ~4–5-Å local resolutions (*14, 15*). However, Sec62 and the ER-luminal J-domain of Sec63, which transiently interacts with BiP (*9-11, 16*), were not sufficiently resolved for model building, likely due to their flexible motions (Fig. 1A). The structure reveals that Sec63 together with Sec71-72 forms a large soluble domain, which sits on the cytosolic side of the Sec61 channel (Fig. 1). Sec63 consists of an N-terminal domain containing 3 TMs and a J-domain between the second and third TMs, and a C-terminal cytosolic domain (Fig. 2, A and B). The cytosolic domain contains two α-helical domains (HD1 and HD2) and an immunoglobulin-like (fibronectin type-III; shortly FN3) domain, which are arranged similarly to the homologous region of the Brr2 RNA helicase (*17*) (fig. S3). Sec71-Sec72, the structure of which is similar to a recent crystal structure of *Chaetomium thermophilum* Sec71-72 (*18*), clamps Sec63's cytosolic domain like 'tongs' (fig. S4).

Sec63 makes extensive contacts with the channel through its transmembrane, cytosolic, and luminal domains, indicative of a major role in regulating the channel's function (Fig. 2 C–E). In the membrane region, the TMs of Sec63 are located at the back (opposite from the lateral gate) of the Sec61 channel, interacting with the TMs of Sec61β and Sec61γ as well as TM1 and TM5 of Sec61α (Fig. 2C). Considering the extensive interactions between these elements, the TMs of Sec63 likely makes a main contribution to the association between Sec61 and the rest of the Sec complex. In the cytosolic region, the FN3 domain of Sec63 interacts with the loop between TM6 and TM7 (L6/7) of Sec61α through antigen-antibody-like binding. Like other FN3 domains, FN3 of Sec63 has a canonical β-sandwich fold comprised of 7 β-stands (referred to as A to G) but contains unusually long A-B, B-C, and D-E inter-strand loops (fig. S3 B and C). With both A-B and B-C loops, FN3 creates a binding surface for L6/7 using a combination of surface complementarity and electrostatic and hydrophobic interactions (Fig. 2E, and fig. S3D). Although sequence conservation is not obvious, metazoan Sec63s have similar extensions in the A-B and B-C loops. We expect analogous interactions between Sec63 and Sec61 in other eukaryotes. The interaction between FN3 and L6/7 is noteworthy because L6/7, together with L8/9, forms a docking site for the

ribosome (*14, 19, 20*) (fig. S5A). Accordingly, superimposition of the Sec complex with a ribosome-bound Sec61 structure shows massive steric clashes between the ribosome and the cytosolic domains of Sec63 and Sec62 (fig. S5B), explaining why Sec61 in the Sec complex cannot bind to the ribosome (*7, 11*). In the ER luminal side, a segment preceding TM3 of Sec63 is directed into the luminal funnel of the Sec61 channel through the crevice present between TM5 of Sec61α and the TM of Sec61γ (Fig. 2D). Notably, this segment makes an antiparallel β-sheet together with a β-hairpin looping out in the middle of Sec61α's TM5. This β-augmentation is further buttressed by hydrophobic interactions with the N-terminal segment of Sec63. These features are highly conserved throughout eukaryotes and thus likely play an important role in optimal positioning of the J-domain.

One striking feature of the Sec complex structure is a fully open channel (Fig. 3, A and B). The Sec61/SecY channel has a characteristic 'clamshell'-like topology, in which its central pore can open towards the lipid phase through the lateral gate formed between TM2 and TM7. Compared to previous Sec61/SecY structures (*4, 14, 21-24*), the channel in the Sec complex displays a substantially wider opening at its lateral gate, through which a signal sequence can readily pass as an α-helix. (Fig. 3, and fig. S6). This contrasts with structures of channels associated with the ribosome or the bacterial posttranslational translocation motor SecA (*14, 21-24*), where the channel shows an only partially open lateral gate (Fig. 3, C–F), which was proposed to be further opened by interaction with the hydrophobic signal sequence during the initial substrate insertion. The opening is achieved by a largely rigid-body movement between the two halves (TMs 1–5 and 6–10) of Sec61α and additional motions of the lateral gate helices. The fully open conformation appears to be a result of the extensive interactions with Sec63. For example, binding between FN3 and L6/7 perhaps pulls the C-terminal half of Sec61α to open the lateral gate. However, further investigation will be necessary to understand the precise mechanism and the dynamics of channel gating in the native membrane environment. At the open lateral gate slit, there is a weak density feature, which likely represents bound detergent molecules (Fig. 3, A and B). In the native membrane, lipid molecules may occupy this site and facilitate initial binding of signal sequences.

Our channel structure likely also represents a fully open state of the translocation pore (Fig. 3B, and fig. S7). The radius of the pore constriction is ~3 Å, large enough to readily pass an extended polypeptide chain. The opening would also permit passage of small hydrated ions and polar molecules in the absence of a translocating polypeptide (*25, 26*), although the relatively positive electrostatic potential around the pore may disfavor permeation of positively charged species (fig. S7C). Yeast Sec61 has a relatively less hydrophobic pore constriction compared to non-fungal Sec61 and prokaryotic SecY (fig. S7D). In prokaryotes, reduction of hydrophobicity in the pore constriction has been shown to lead to membrane potential dissipation (*26*), and similarly, in higher eukaryotes it might cause calcium leakage from ER. However, yeast may tolerate ion leakage because calcium is stored primarily in the vacuole. In resting or primed channels, the pore is closed or narrow (<2 Å in radius), and further blocked by a small α-helical plug in the luminal funnel (*4, 14, 21*). By contrast, in our structure the plug seems flexible and displaced from the pore (Fig 3, A and B).

The spatial arrangement of Sec63 and Sec71-72 with respect to the Sec61 channel suggests how these components play roles in accepting a polypeptide substrate from a cytosolic chaperone and handing it over to the channel and subsequently to BiP. Studies of *C. thermophilum* Sec72 have suggested that Sec72 provides a docking site for the cytosolic Hsp70 chaperone Ssa1p (*18*), which prevents substrates from premature folding or aggregation before translocation (*6*). Superimposition of the co-crystal structure of Sec72 and an Ssa1p C-terminal tail shows that the Ssa1p-binding site is ~60 Å above the

channel's pore (Fig. 4A). While the cytosolic domain of Sec63-71-72 sits on top of Sec61, its position is tilted such that the polypeptide can insert straight down to the pore. Similarly, Sec62 is also positioned off the translocation path (Fig. 1A). Therefore, upon release from Ssa1p, a substrate would efficiently engage with the pore without obstruction. The structure also allows us to propose how BiP Hsp70 may catch the substrate in the ER lumen. Despite the low resolution of the J-domain (Fig. 1A), we could dock a homology model into the EM density map based on the shape of the feature and the orientations of the flanking segments (Fig. 4A). We then superimposed a recent crystal structure of a bacterial J-domain–Hsp70 complex (*27*) to our EM structure (Fig. 4A). Strikingly, this modeling exercise showed a peptide binding cleft of the Hsp70 (called substrate-binding domain β or SBDβ) is placed directly below the translocation pore. Thus, the J-domain seems optimally positioned to allow BiP to grasp the substrate polypeptide as it emerges from the channel.

Our structure offers a model for how Sec63 enables posttranslational translocation (Fig. 4B, and fig. S8) and provides a more complete picture of how the Sec61/SecY channel works together with different binding partners (i.e., ribosomes, Sec63, or SecA) to enable transport of a range of substrates. Association of Sec63 seems to induce full opening of the channel, a conformation in which the channel can readily accept a substrate polypeptide. Such a conformation, compared to a partially open channel seen with the other modes, is likely advantageous for many posttranslational-specific substrates, which tend to have a less hydrophobic signal sequence (*28-30*).

Figure Captions

Figure 1. Structure of the yeast Sec complex. Cryo-EM density map (**A**) and atomic model (**B**) of the yeast posttranslational protein translocation complex. Front view, view into the lateral gate.

Figure 2. Structure of Sec63 and interactions with the channel. (**A**) A schematic of Sec63 domains. Regions interacting with other parts of the complex are indicated by blue lines. Unmodeled regions are shown in dashed lines. (**B**) Structure of Sec63 (front view). The position of Sec61 is shown by a gray shade. (**C**) Interactions between TMs of Sec63 and Sec61. Left, a view from the back; right, a cutaway view from the ER lumen. Black arrowed line, the cross-sectional plane. Note that TMs 2, 9, and 10 of Sec61α are located above the cross-sectional plane. (**D**) Interactions between Sec63 and Sec61 in the luminal side. Left, a β-sheet formed between Sec61α (TM5 indicated by a dashed line) and the segment between Sec63 TM3 and the J-domain. Right, a magnified view with side chains in sticks. (**E**) Interactions between the FN3 domain and the cytosolic loop L6/7 of Sec61α (also see Fig. 1B).

Figure 3. A fully opened Sec61 channel in the Sec complex. (**A** and **B**) Structure of the Sec61 channel. The N- and C- terminal halves of Sec61α are in blue and salmon, respectively. Gray density feature is presumed detergent molecules. Pore-lining residues are shown as green balls and sticks. Density feature for the plug is in purple. '2' and '7' indicate TM2 and TM7 respectively. (**C**–**F**) Comparison of Sec61 of the Sec complex (colored) with Sec61 of the cotranslational ribosome-Sec61 complex (gray; C and D) or SecY of a bacterial posttranslational SecA-SecY channel complex (gray; E and F). The structures are aligned with respect to the C-terminal half of Sec61α (C–F). Shown are the front (A, C, and E) and cytosolic (B, D, and F) views. Numbers indicate corresponding TMs. Dashed line, lateral gate. Asterisk, translocation pore. For simplicity, L6/7 and L8/9 of Sec61α were not shown. In D and F, TMs of Sec63 are also shown (green). Also see fig. S6 for comparisons to archaeal SecY and substrate-engaged channels.

Figure 4. Model of an active translocation complex. (**A**) The Sec complex structure superimposed with a Ssa1p C-terminal peptide (red orange; PDB ID: 5L0Y) and DnaK Hsp70 as a model for BiP (yellow and brown; PDB ID: 5RNO). (**B**) Schematics for a closed Sec61 channel in isolation (left), an open channel in association with Sec63 (middle), and an active Sec complex engaged with a substrate (right; corresponding to the model in (A)). For the full translocation cycle, see fig S8.

References and Notes

1. E. Park, T. A. Rapoport, Mechanisms of Sec61/SecY-mediated protein translocation across membranes. *Annu Rev Biophys* **41**, 21-40 (2012).
2. R. M. Voorhees, R. S. Hegde, Toward a structural understanding of co-translational protein translocation. *Curr Opin Cell Biol* **41**, 91-99 (2016).
3. E. C. Mandon, S. F. Trueman, R. Gilmore, Protein translocation across the rough endoplasmic reticulum. *Cold Spring Harb Perspect Biol* **5**, (2013).
4. B. Van den Berg *et al.*, X-ray structure of a protein-conducting channel. *Nature* **427**, 36-44 (2004).
5. J. A. Rothblatt, R. J. Deshaies, S. L. Sanders, G. Daum, R. Schekman, Multiple genes are required for proper insertion of secretory proteins into the endoplasmic reticulum in yeast. *J Cell Biol* **109**, 2641-2652 (1989).

6. R. J. Deshaies, S. L. Sanders, D. A. Feldheim, R. Schekman, Assembly of yeast Sec proteins involved in translocation into the endoplasmic reticulum into a membrane-bound multisubunit complex. *Nature* **349**, 806-808 (1991).
7. H. A. Meyer *et al.*, Mammalian Sec61 is associated with Sec62 and Sec63. *J Biol Chem* **275**, 14550-14557 (2000).
8. J. Tyedmers *et al.*, Homologs of the yeast Sec complex subunits Sec62p and Sec63p are abundant proteins in dog pancreas microsomes. *Proc Natl Acad Sci U S A* **97**, 7214-7219 (2000).
9. D. Feldheim, J. Rothblatt, R. Schekman, Topology and functional domains of Sec63p, an endoplasmic reticulum membrane protein required for secretory protein translocation. *Mol Cell Biol* **12**, 3288-3296 (1992).
10. J. L. Brodsky, R. Schekman, A Sec63p-BiP complex from yeast is required for protein translocation in a reconstituted proteoliposome. *J Cell Biol* **123**, 1355-1363 (1993).
11. S. Panzner, L. Dreier, E. Hartmann, S. Kostka, T. A. Rapoport, Posttranslational protein transport in yeast reconstituted with a purified complex of Sec proteins and Kar2p. *Cell* **81**, 561-570 (1995).
12. K. E. Matlack, B. Misselwitz, K. Plath, T. A. Rapoport, BiP acts as a molecular ratchet during posttranslational transport of prepro-alpha factor across the ER membrane. *Cell* **97**, 553-564 (1999).
13. N. Green, H. Fang, P. Walter, Mutants in three novel complementation groups inhibit membrane protein insertion into and soluble protein translocation across the endoplasmic reticulum membrane of Saccharomyces cerevisiae. *J Cell Biol* **116**, 597-604 (1992).
14. R. M. Voorhees, I. S. Fernandez, S. H. Scheres, R. S. Hegde, Structure of the mammalian ribosome-Sec61 complex to 3.4 A resolution. *Cell* **157**, 1632-1643 (2014).
15. K. Braunger *et al.*, Structural basis for coupling protein transport and N-glycosylation at the mammalian endoplasmic reticulum. *Science* **360**, 215-219 (2018).
16. K. E. Matlack, K. Plath, B. Misselwitz, T. A. Rapoport, Protein transport by purified yeast Sec complex and Kar2p without membranes. *Science* **277**, 938-941 (1997).
17. T. H. Nguyen *et al.*, Structural basis of Brr2-Prp8 interactions and implications for U5 snRNP biogenesis and the spliceosome active site. *Structure* **21**, 910-919 (2013).
18. A. Tripathi, E. C. Mandon, R. Gilmore, T. A. Rapoport, Two alternative binding mechanisms connect the protein translocation Sec71-Sec72 complex with heat shock proteins. *J Biol Chem* **292**, 8007-8018 (2017).
19. Z. Cheng, Y. Jiang, E. C. Mandon, R. Gilmore, Identification of cytoplasmic residues of Sec61p involved in ribosome binding and cotranslational translocation. *J Cell Biol* **168**, 67-77 (2005).
20. T. Becker *et al.*, Structure of monomeric yeast and mammalian Sec61 complexes interacting with the translating ribosome. *Science* **326**, 1369-1373 (2009).
21. J. Zimmer, Y. Nam, T. A. Rapoport, Structure of a complex of the ATPase SecA and the protein-translocation channel. *Nature* **455**, 936-943 (2008).
22. P. F. Egea, R. M. Stroud, Lateral opening of a translocon upon entry of protein suggests the mechanism of insertion into membranes. *Proc Natl Acad Sci U S A* **107**, 17182-17187 (2010).
23. R. M. Voorhees, R. S. Hegde, Structure of the Sec61 channel opened by a signal sequence. *Science* **351**, 88-91 (2016).
24. L. Li *et al.*, Crystal structure of a substrate-engaged SecY protein-translocation channel. *Nature* **531**, 395-399 (2016).
25. D. Heritage, W. F. Wonderlin, Translocon pores in the endoplasmic reticulum are permeable to a neutral, polar molecule. *J Biol Chem* **276**, 22655-22662 (2001).
26. E. Park, T. A. Rapoport, Preserving the membrane barrier for small molecules during bacterial protein translocation. *Nature* **473**, 239-242 (2011).

27. R. Kityk, J. Kopp, M. P. Mayer, Molecular Mechanism of J-Domain-Triggered ATP Hydrolysis by Hsp70 Chaperones. *Mol Cell* **69**, 227-237 e224 (2018).
28. D. T. Ng, J. D. Brown, P. Walter, Signal sequences specify the targeting route to the endoplasmic reticulum membrane. *J Cell Biol* **134**, 269-278 (1996).
29. M. A. Smith, W. M. Clemons, Jr., C. J. DeMars, A. M. Flower, Modeling the effects of prl mutations on the Escherichia coli SecY complex. *J Bacteriol* **187**, 6454-6465 (2005).
30. S. F. Trueman, E. C. Mandon, R. Gilmore, A gating motif in the translocation channel sets the hydrophobicity threshold for signal sequence function. *J Cell Biol* **199**, 907-918 (2012).
31. D. N. Mastronarde, Automated electron microscope tomography using robust prediction of specimen movements. *J Struct Biol* **152**, 36-51 (2005).
32. S. Q. Zheng *et al.*, MotionCor2: anisotropic correction of beam-induced motion for improved cryo-electron microscopy. *Nat Methods* **14**, 331-332 (2017).
33. A. Punjani, J. L. Rubinstein, D. J. Fleet, M. A. Brubaker, cryoSPARC: algorithms for rapid unsupervised cryo-EM structure determination. *Nat Methods* **14**, 290-296 (2017).
34. A. Rohou, N. Grigorieff, CTFFIND4: Fast and accurate defocus estimation from electron micrographs. *J Struct Biol* **192**, 216-221 (2015).
35. P. Emsley, B. Lohkamp, W. G. Scott, K. Cowtan, Features and development of Coot. *Acta Crystallogr D Biol Crystallogr* **66**, 486-501 (2010).
36. P. V. Afonine *et al.*, Real-space refinement in PHENIX for cryo-EM and crystallography. *Acta Crystallogr D Struct Biol* **74**, 531-544 (2018).
37. V. B. Chen *et al.*, MolProbity: all-atom structure validation for macromolecular crystallography. *Acta Crystallogr D Biol Crystallogr* **66**, 12-21 (2010).
38. B. A. Barad *et al.*, EMRinger: side chain-directed model and map validation for 3D cryo-electron microscopy. *Nat Methods* **12**, 943-946 (2015).
39. N. A. Baker, D. Sept, S. Joseph, M. J. Holst, J. A. McCammon, Electrostatics of nanosystems: application to microtubules and the ribosome. *Proc Natl Acad Sci U S A* **98**, 10037-10041 (2001).
40. E. F. Pettersen *et al.*, UCSF Chimera--a visualization system for exploratory research and analysis. *J Comput Chem* **25**, 1605-1612 (2004).

Acknowledgments: We thank D. Toso for help with electron microscope operation, and J. Hurley, S. Brohawn, and K. Tucker for critical reading of manuscript. **Funding:** This work was funded by UC Berkeley (E.P.) and an NIH training grant (T32GM008295; S.I.). **Author contributions:** S.I. and E.P performed experiments, interpreted results, and wrote the manuscript; E.P. conceived and supervised the project. **Competing interests:** None declared. **Data and materials availability:** The cryo-EM density maps and atomic model have been deposited in EM Data Bank (accession code: EMD-0336) and Protein Data Bank (accession code: 6N3Q), respectively.

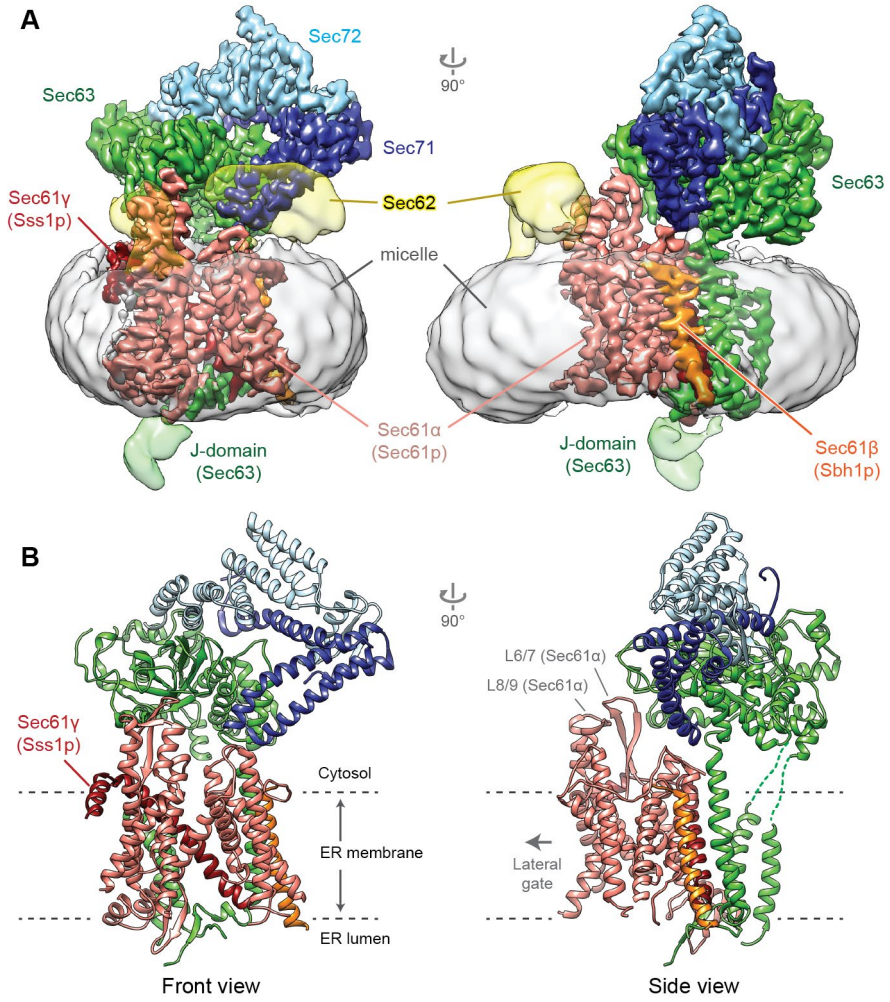
A
Sec72
Sec63
Sec71
Sec62
Sec61γ
(Sss1p)
micelle
90°
Sec63
Sec61α
(Sec61p)
J-domain
(Sec63)
J-domain
(Sec63)
Sec61β
(Sbh1p)
B
90°
Sec61γ
(Sss1p)
Cytosol
ER membrane
ER lumen
L6/7 (Sec61α)
L8/9 (Sec61α)
Lateral
gate
Front view
Side view

Fig. 1

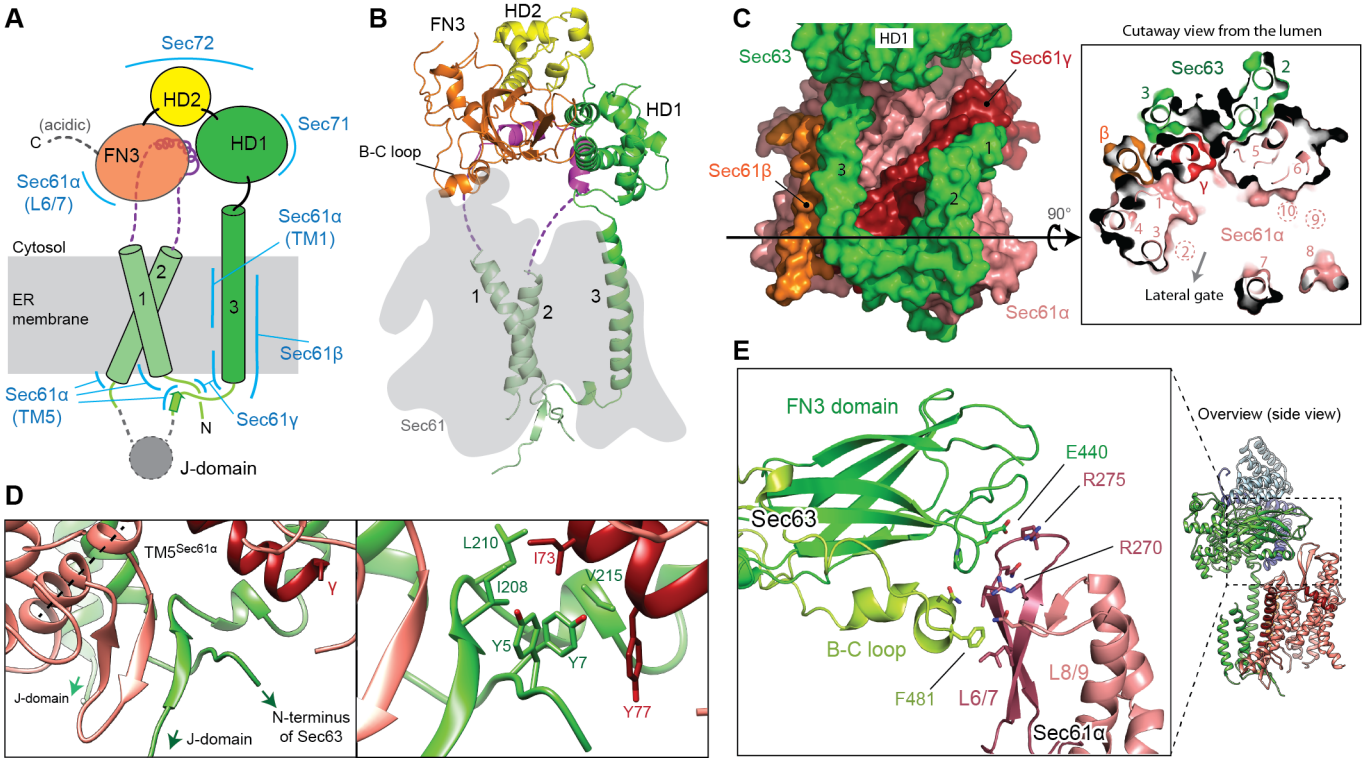
A
Sec72
HD2
(acidic)
C
FN3
HD1
Sec71
Sec61α
(L6/7)
Cytosol
Sec61α
(TM1)
ER
membrane
1
2
3
Sec61β
Sec61α
(TM5)
N
Sec61γ
J-domain
B
FN3
HD2
HD1
B-C loop
1
2
3
Sec61
C
HD1
Sec63
Sec61γ
Sec61β
3
1
2
90°
Sec61α
Cutaway view from the lumen
Sec63
2
3
1
β
γ
Sec61α
Lateral gate
D
TM5Sec61α
γ
J-domain
J-domain
N-terminus
of Sec63
L210
I73
I208
V215
Y5
Y7
Y77
E
FN3 domain
E440
R275
Sec63
R270
B-C loop
L8/9
F481
L6/7
Sec61α
Overview (side view)

Fig. 2

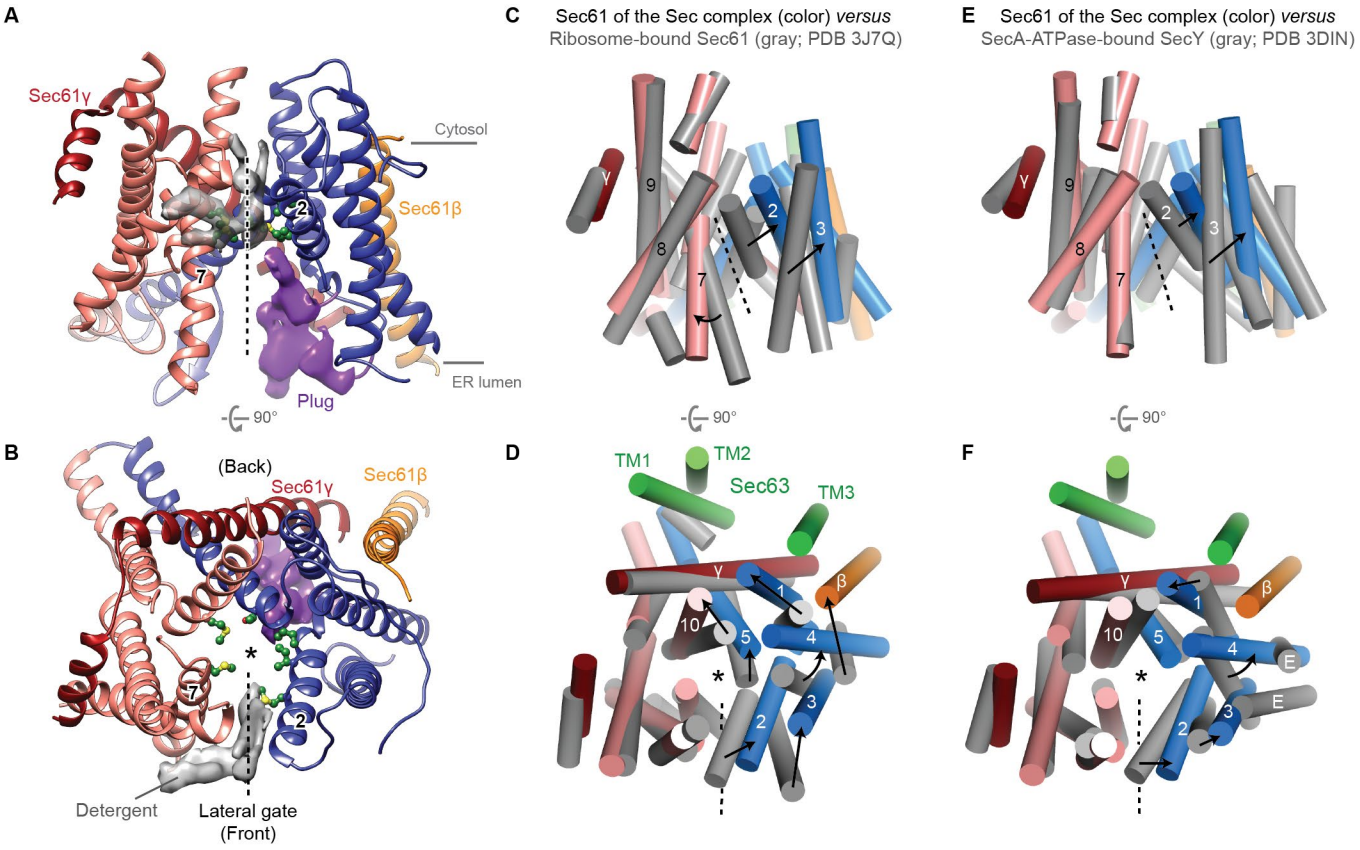
A
Sec61γ
Cytosol
Sec61β
Plug
ER lumen
90°
B
(Back)
Sec61γ
Sec61β
Detergent
Lateral gate
(Front)
C
Sec61 of the Sec complex (color) *versus*
Ribosome-bound Sec61 (gray; PDB 3J7Q)
90°
D
TM1
TM2
Sec63
TM3
E
Sec61 of the Sec complex (color) *versus*
SecA-ATPase-bound SecY (gray; PDB 3DIN)
90°
F

Fig. 3

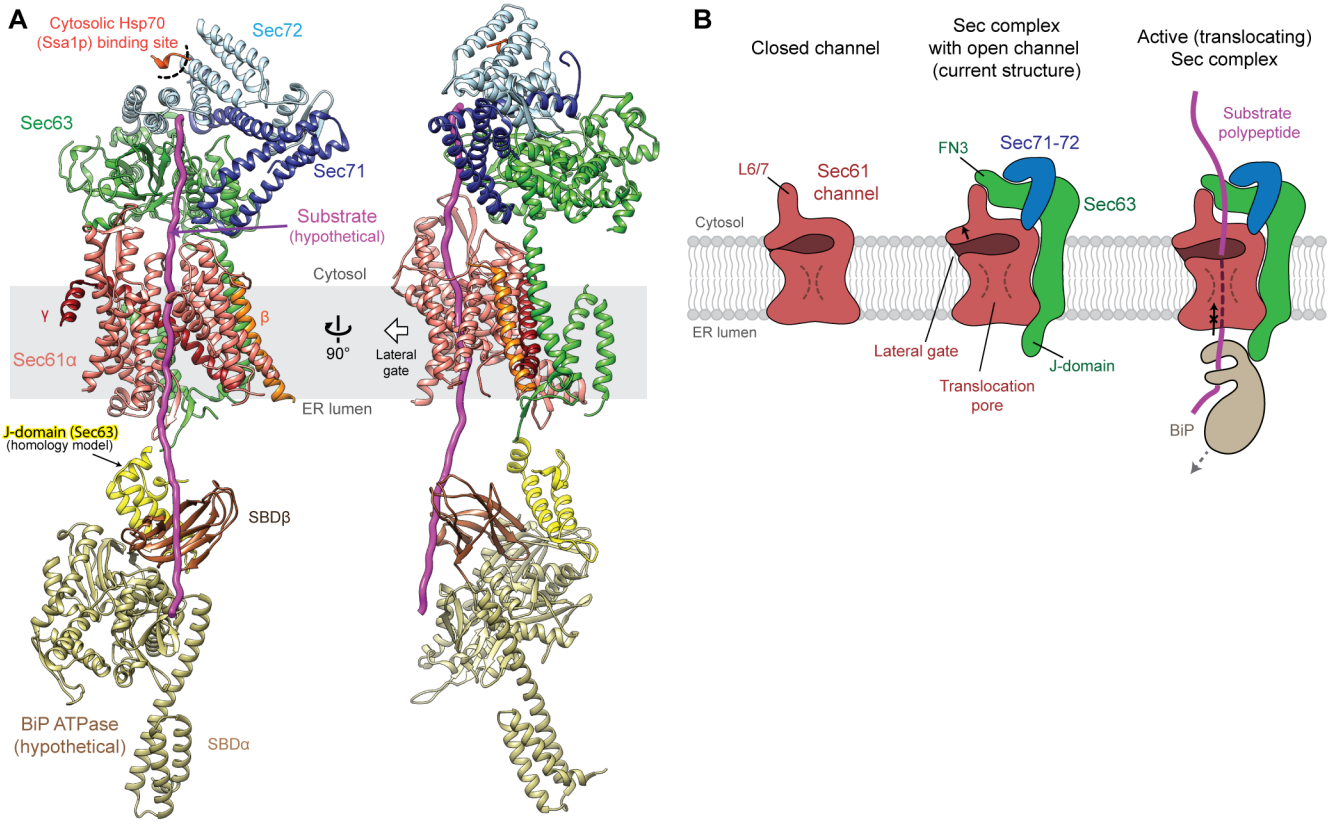
A
Cytosolic Hsp70
(Ssa1p) binding site
Sec72
Sec63
Sec71
Substrate
(hypothetical)
Cytosol
γ
β
Sec61α
90°
Lateral
gate
ER lumen
J-domain (Sec63)
(homology model)
SBDβ
BiP ATPase
(hypothetical)
SBDα
B
Closed channel
Sec complex
with open channel
(current structure)
Active (translocating)
Sec complex
Substrate
polypeptide
L6/7
Sec61
channel
FN3
Sec71-72
Sec63
Cytosol
ER lumen
Lateral gate
Translocation
pore
J-domain
BiP

Fig. 4

Supplementary Materials for

Structure of the posttranslational Sec protein-translocation channel complex from yeast

Samuel Itskanov and Eunyong Park

correspondence to: eunyong_park@berkeley.edu

This PDF file includes:

Materials and Methods

Construction of plasmids and yeast strains

To enable efficient purification of the endogenous heptameric Sec complex from yeast, *Saccharomyces cerevisiae* strain BY4741 was modified to encode the fusion protein of Sbh1p (Sec61β)–Sec63p–GFP (green fluorescent protein) from the *SEC63* locus. In addition, the fusion construct contains a 15-amino-acid Gly/Ser linker between Sbh1p and Sec63p (amino acid sequence: …GKLF (Sbh1p)–GGSGGSGGSGGSGGS (linker)–PTNY…(Sec63p)) and a tobacco etch virus (TEV) protease cleavage site between Sec63 and GFP (amino acid sequence: …ESPE (Sec63p)–AGGATTASGTG (linker)–ENLYFQG (TEV site)–TASGGGS (linker)–KGEELF…(GFP)). To attach the GFP tag to the C-terminus of Sec63p, a PCR product was generated to contain a 50-bp 5' homology arm (immediately before the *SEC63* stop codon; 5'-at act gat atc gat acg gat aca gaa gct gaa gat gat gaa tca cca gaa-3'), TEV, GFP, a nourseothricin resistance cassette, and a 50-bp 3' homology arm (downstream of *SEC63*; 5'-cat ttt agc tct tag acg tat ata ttt cat ctt tat aaa aat aga tac at-3'). DNA was introduced to yeast cells by a standard lithium acetate/polyethylene glycol transformation protocol, and the cells were placed on a YPD agar medium (1% yeast extract, 2% peptone, 2% glucose, and 2% bacto-agar) containing 100 μg/mL nourseothricin. Colonies were isolated after 2 days at 30°C and recombination was confirmed by PCR. Fusion of Sbh1p and Sec63 was carried out similarly. We first generated a pGEM vector containing a ~3-kb genomic fragment in the *SEC63* (~2kb upstream and ~1kb downstream of the *SEC63* start codon), and then the *OSW1* gene (upstream of SEC63) was replaced with hygromycin resistance cassette. This was then followed by insertion of the *SBH1* coding sequence and a Gly/Ser linker immediately upstream of the *SEC63* start codon). The resulting pGEM was linearized by restriction enzymes and used for transformation. Integration of the Sbh1p-encoding segment was confirmed using Sanger sequencing. The endogenous copy of *SBH1* was replaced with a G418 resistance marker (5'-homology arm: 5'-ggg aaa aga ttt caa cca cca ctt caa aac acc aca ctc tac ctc cta cca tac tcc ata-3'; 3'-homology arm: 5'-taa gaa ttt tct tca gta atg att cag ctt tta tcc acc cta ttt gac aaa aca aga cta-3') and the deletion was confirmed by PCR. The resulting strain grew comparably to the wild-type, indicating that the fusion does not interfere with protein translocation *in vivo*. In addition to the fusion, we also slightly overexpressed the remaining five subunits of the heptameric complex (Sec61p, Sss1p, Sec62p, Sec71p and Sec72p) using a yeast CEN-ARS plasmid (with a URA marker) containing each gene (under their own endogenous promoter) in tandem. We note that transformation of this plasmid did not significantly change the band intensities of subunits in SDS-PAGE (data not shown), suggesting that Sec63 was already saturated without the plasmid.

Protein purification

Yeast cells were grown in YPD medium (1% yeast extract, 2% peptone, and 2% glucose) in shaker flasks at 30 °C. Upon reaching an optical density (OD600) of ~3, cells were harvested by centrifugation at 4,600g for 10 min. Cell pellets were frozen in liquid nitrogen and stored in −80 °C until use. Cell lysis was performed by cryo-milling (SPEX SamplePrep) at liquid-nitrogen temperature. All subsequent steps were carried out at 4 °C. Pulverized cells were resuspended in buffer containing 50 mM Tris pH 7.5, 200 mM

NaCl, 1 mM EDTA, 10% glycerol, 2mM DTT, 5 μg/ml aprotinin, 5 μg/ml leupeptin, 1 μg/ml pepstatin A, and 1.2 mM PMSF. To solubilize membranes, 1% lauryl maltose neopentyl glycol (LMNG; Anatrace) and 0.2% cholesteryl hemisuccinate (CHS; Anatrace) were added to the cell lysate. After 1.5-h incubation, the lysate was then clarified by ultracentrifugation (Beckman Type 45 Ti rotor) at 125,000g for 1 h. The clarified lysate was incubated by gentle rotation with agarose beads conjugated with anti-GFP nanobody (Chromotek) for 2.5 h. The beads were then packed in a gravity column and washed with approximately 20 column volumes of buffer containing 50 mM Tris pH 7.5, 200mM NaCl, 1.0 mM EDTA, 2 mM DTT, 0.02% glycol-diosgenin (GDN; Anatrace), and 10% glycerol. The Sec complex was eluted by incubating the beads with ~10 μg/mL TEV protease (approximately 1:15 weight ratio to the Sec complex) for ~14 h. The eluate was concentrated using an AmiconUltra centrifugal filter (100-kDa cut-off; Millipore) and injected into a Superose 6 Increase column (GE Lifesciences) equilibrated with 20 mM Tris pH 7.5, 100 mM NaCl, 1mM EDTA, 2 mM DTT, and 0.02% GDN. Peak fractions were pooled and concentrated to ~5 mg/mL. The sample was immediately used for cryo-EM grid preparation.

Cryo-EM analysis

Right before grid freezing, 3 mM fluorinated Fos-Choline-8 (FFC8; Anatrace) was added to the purified Sec complex. Gold Quantifoil R 1.2/1.3 holey carbon grid (Quantifoil) was glow-discharged for 20 s in Ar/O2 (75%:25%) using a Gatan Solarus plasma cleaner or in air using a PELCO easiGlow glow discharge cleaner. 3 μL of the sample were applied to a glow-discharged grid. After incubating at 4 °C and 100% humidity for 10 s, the grid was blotted with Whatman No. 1 filter papers for 3 s and plunge-frozen in liquid-nitrogen-cooled liquid ethane using Vitrobot Mark IV (FEI).

The data sets were collected on an FEI Talos Arctica electron microscope operated at an acceleration voltage of 200 kV (table S1). Dose-fractionated images (movies) were recorded on a Gatan K2 Summit direct electron detector operated in the super-resolution mode (with a physical pixel size of 1.16 Å) using SerialEM software (*31*). The total exposure was 8 s at a frame rate of 0.2 s/frame and a dose rate of 1.25 e^- per $Å^2$ per frame. Target defocus values were from −0.8 μm to −2.4 μm.

A summary of the single-particle analysis procedure is shown in fig. S1. First, the movies were subjected to whole-frame-only motion correction using MotionCor2 (*32*). The corrected movies were then 2x frame-binned by averaging each two frames, resulting in a total of 20 frames per movie. All subsequent image processing was performed using cryoSPARC v2 (*33*). Defocus values were estimated on the summed micrographs using CTFFIND4 (*34*) implemented in cryoSPARC. Micrographs that were not suitable for image analysis (containing crystalline ice and displaying large motion drifts) were removed by manual inspection (resulting in 2,162 movies). After automatically picking particles (407,288 particles), the particles were polished by per-particle motion correction with the 2x frame-binned movies (358,961 particles; the remaining particles were rejected due to proximity to the micrograph edges). The particle images were extracted with a box size of 256 pixels. The particle images were then subjected to reference-free 2D classification. After removing empty detergent micelle particles, which constituted the majority of discarded particles, and low-quality particles, 208,049 particles were selected. These particles were used for generation of three initial models (ab-initio

reconstruction), followed by 3D classification (heterogeneous refinement). About 83% of the particles populated one class that reached 4.75-Å resolution and showed prominent features of the Sec complex. The particles from this class was further refined by non-uniform refinement of cryoSPARC, leading to the final map at 3.68-Å resolution (based on gold-standard Fourier shell correlation (FSC) of independently refined half maps and the 0.143 cut-off criterion; fig. S2A). Local resolution estimation was also performed in cryoSPARC (fig. S2B). The map shown in figures is a combined map, which was sharpened (B-factor of −104.7 Å2) and lowpass-filtered at 3.68 Å, except for the density map for Sec62, the J-domain, and the detergent micelle (Fig. 1A), which were lowpass-filtered according to local resolution values.

Atomic model building and model refinement

The atomic model was built using Coot (*35*) and the sharpened, lowpass-filtered combined map. The models for Sec61 and Sec63 were built de novo, except for some parts of Sec61α (TM2 and TM7) where prior structural information from the *Methanocaldococcus jannaschii* (PDB ID: 1RH5) and *Pyrococcus furiosus* (PDB ID: 3MP7) SecY channel structures were used. An initial model for Sec71-72 was generated by the SWISS-MODEL homology modeling webserver using the *Chaetomium thermophilum* Sec71-72 crystal structure (PDB ID: 5L0W) as a template, and the model was rebuilt in Coot.

Model refinement was done in real space using Phenix 1.14 (*36*) and the combined map. (table S1). To prevent overfitting, the weight of 2 was used such that when refinement was performed with one of two half maps, the FSC curves between the refined model and either half map (FSC_{work} and FSC_{free}, respectively) do not significantly separate (fig. S2D). We also slightly blurred (by a B-factor of 30 $Å^2$) the lowpass-filtered map prior to model refinement to minimize the fitting into high-frequency noises. The refinement resolution limit was set to 3.7 Å. MolProbity (*37*) and EMRinger (*38*) were used for structural validation (table S1). The following amino acid segments were not modeled because they were either invisible or insufficiently resolved in the density map: N–9, 57–72 (plug), 143–146, 311–359, and 469–480(C) of Sec61α (Sec61p); N-50 of Sec61β (Sbh1p); N–25 of Sec61γ (Sss1p); 37–53, 79–92, 116–201 (J-domain), 551-556 and 613–663(C) of Sec63 (Sec63p); N–68 of Sec71 (Sec66p); and all of Sec62. Protein electrostatics were calculated using the Adaptive Poisson-Boltzmann Solver (www.poissonboltmann.org) (*39*) with default parameters. UCSF Chimera (*40*) and PyMOL (Schrödinger) were used to prepare figures in the paper.

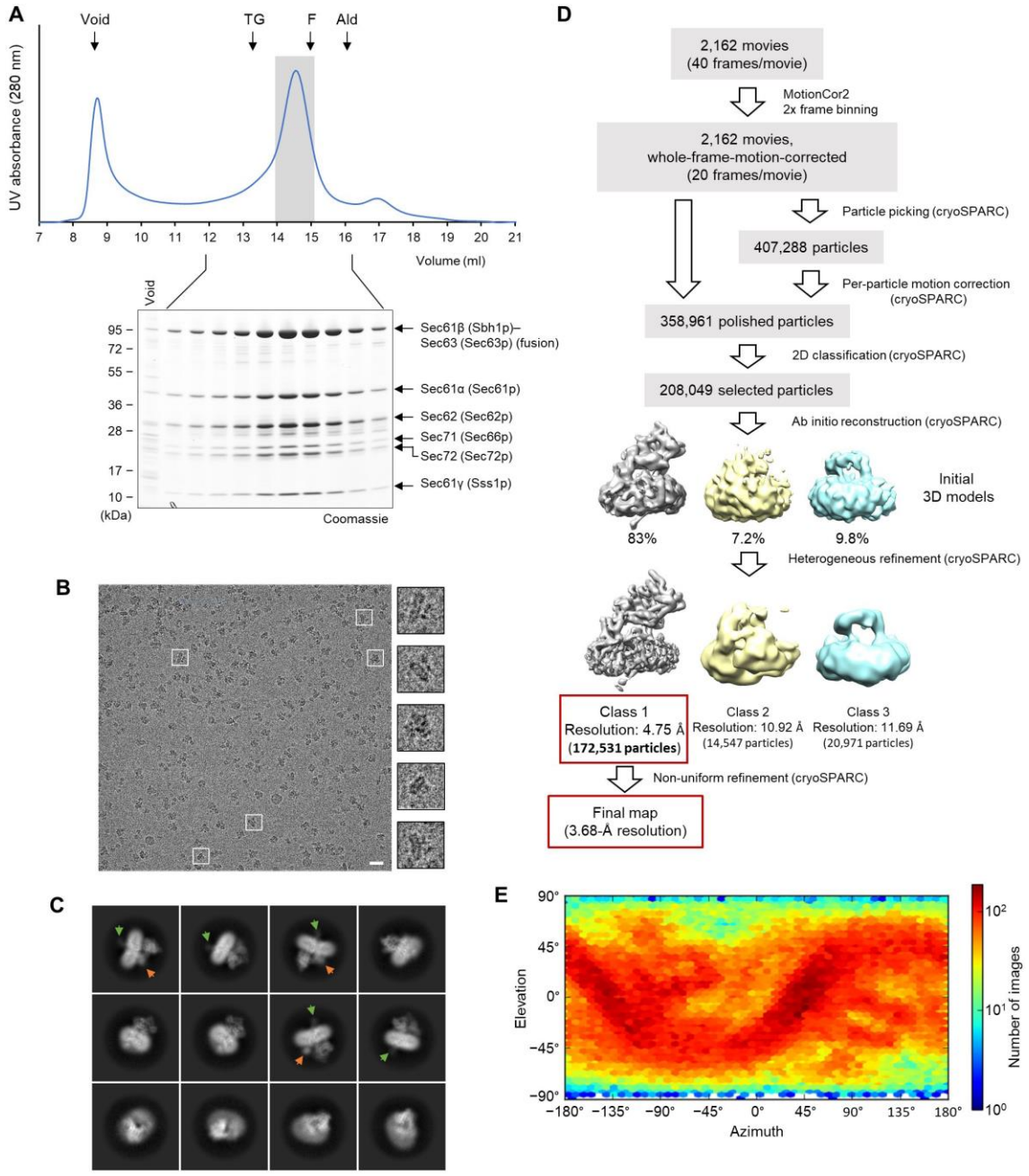

Fig. S1. Purification of the Sec complex and cryo-EM single-particle analysis.

(**A**) Size-exclusion chromatography of the affinity-purified Sec complex. Upper panel, UV absorbance profile of the eluate. Arrowheads indicate the positions of the void peak and molecular weight standards: TG, thyroglobulin (670 kDa); F, ferritin (440 kDa); Ald, aldolase (158 kDa). Lower panel, Coomassie-stained SDS-PAGE gel of the indicated fractions. (**B**) A representative cryo-EM micrograph. Magnified images of particles outlined with white squares are shown in the right panels. Scale bar, 20 nm. (**C**) Selected 2D class averages of particles (box width, 297 Å). Green and orange arrowheads indicate flexible J-domain of Sec63 and cytosolic domain of Sec62. (**D**) Summary of single-particle image analysis procedure. (**E**) Distribution of particle orientations.

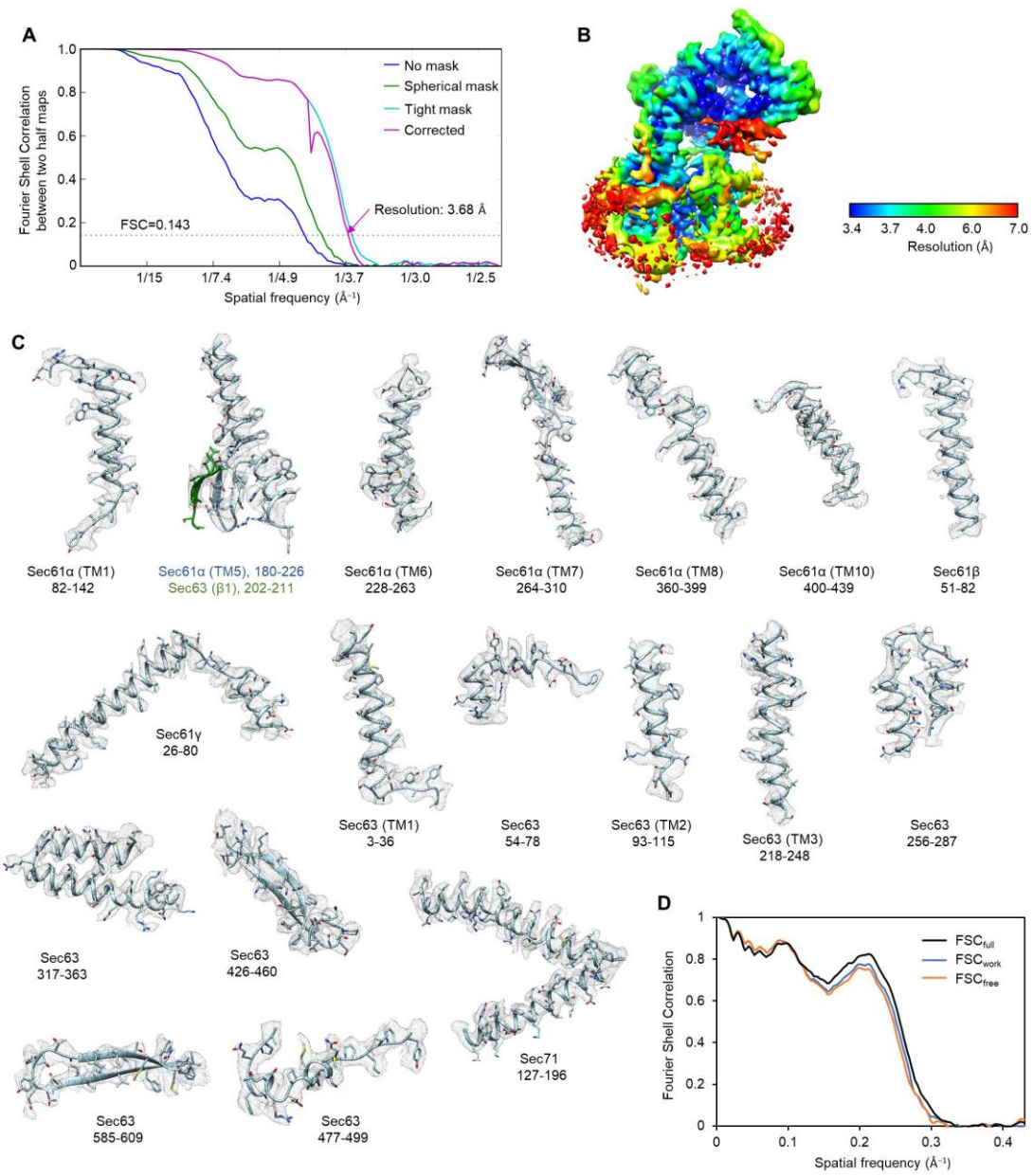

Fig. S2. Quality of the cryo-EM density map and the atomic model.

(**A**) Fourier Shell Correlation (FSC) between the two half maps of the final 3D reconstruction. (**B**) Local resolution map. The shown map is unsharpened, unfiltered map. (**C**) Segments of the atomic model (main chains in ribbon representation and side chains in stick representation) superimposed with the density map (mesh). Positions (amino acid residue numbers) of the segments are indicated. (**D**) FSC between the atomic model and EM maps of the Sec complex. The black curve shows the FSC between the final refined atomic model and the combined map that the model was refined against (FSC_{full}). To prevent overfitting during the model refinement procedure, a test refinement was performed using the first half map. The resulting model was then compared to the first half map (FSC_{work}; blue curve) and the second half map (FSC_{free}; orange curve). The shown refinement was performed using Phenix with a weight of 2.

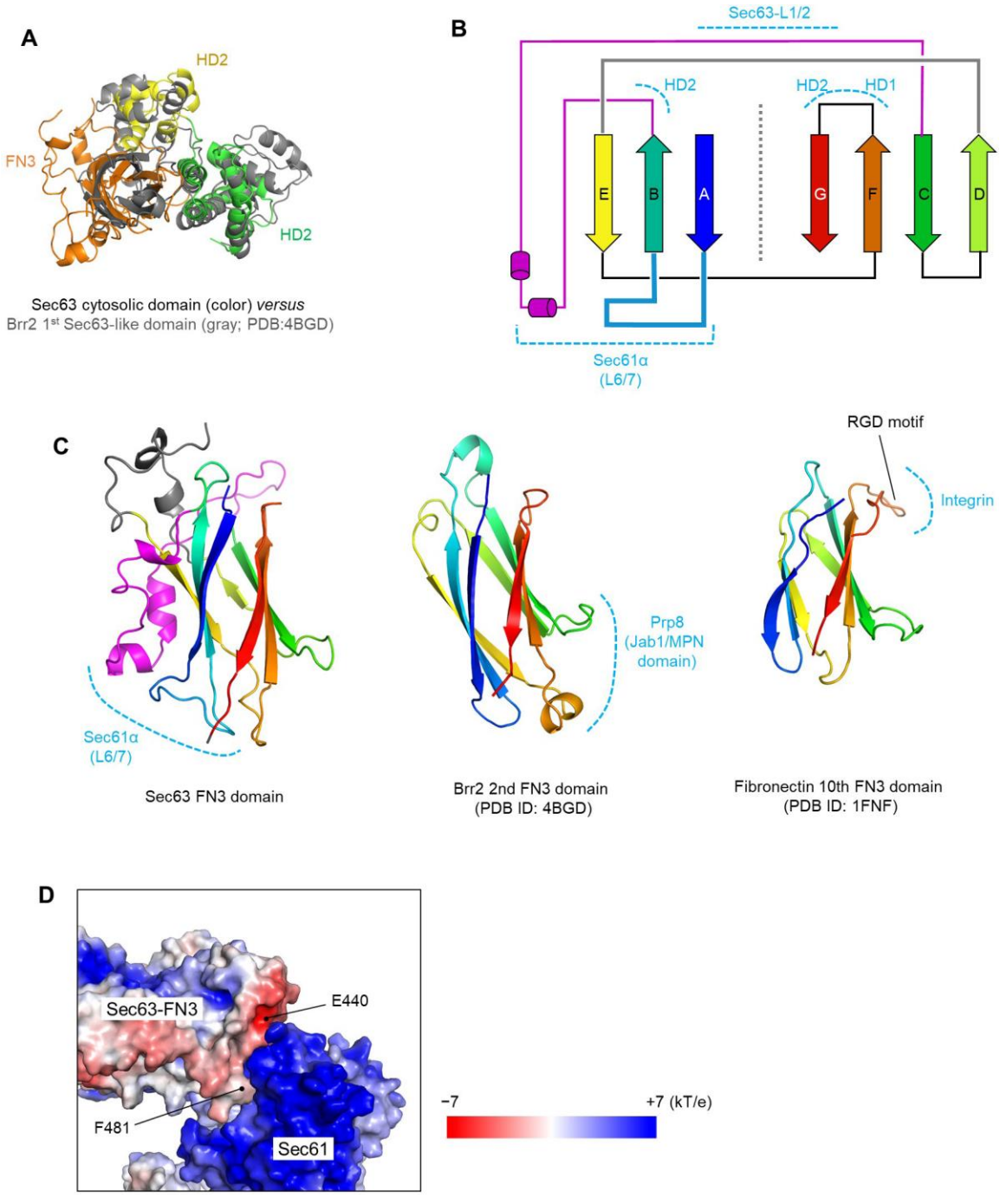

Fig. S3. Structure of the Sec63 FN3 domain.

(**A**) Superimposition between the Sec63 cytosolic domain and Brr2's first Sec63 homology domain (PDB ID: 4BGD) (*17*). Note that full-length Brr2 contains two sets of Sec63 homology domains in addition to two helicase domains. (**B**) Schematic representation of Sec63 fibronectin type-3 (FN3) domain. β sheets are depicted as arrows and two small α-helices in the B-C loop are depicted as cylinders. Regions which interact with other parts of the Sec complex are highlighted with cyan dashed lines. Note that L1/2 refers to the segments between TM1 and TM2 of Sec63. L1/2 contains two short α-

helices arranged in an inversed ‘L’ shape (see Fig 2 A and B; in purple), which interact with the C-terminal cytosolic domain of Sec63. (**C**) Yeast Sec63 FN3 domain (left) was compared to the FN3 domains in yeast Brr2’s first Sec63 homology domain (middle) and in human fibronectin (10^{th} FN3 domain; right). The views are approximately in the same orientation. The color schemes are the same as in (B). Regions involved in protein interactions are highlighted with dashed cyan lines. (**D**) The interaction between the Sec63 FN3 domain and the cytosolic loop L6/7 of Sec61α is shown in a surface representation with electrostatic potential indicated by a color map. The viewing angle is the same as in Fig. 2E.

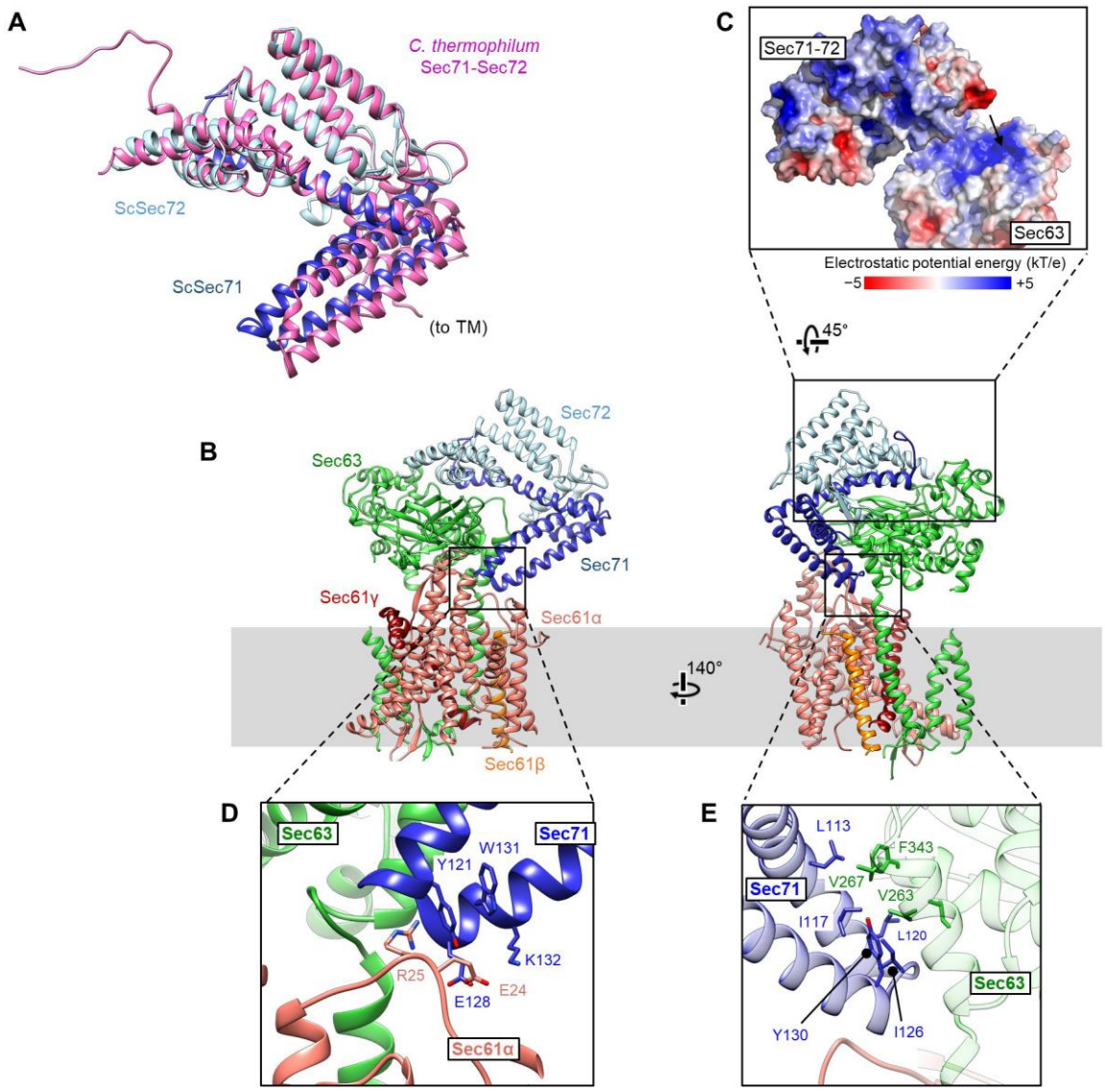

Fig. S4. Structure of Sec71-72 in the Sec complex.

(**A**) Comparison between *S. cerevisiae* Sec71-72 (ScSec71 in blue and ScSec72 in cyan) in the Sec complex and the crystal structure of isolated *C. thermophilum* Sec71-72 (pink; PDB ID: 5L0W) (*18*). (**B**) A ribbon model of the yeast Sec complex. The regions outlined with black lines are magnified and displayed in panels (C–E) to show interactions between Sec71-Sec72 and other subunits. Sec71-72 associates with the cytosolic domain of Sec63 mainly by electrostatic and hydrophobic interactions (see (C) and (E)). Sec71 also form a minor contact with Sec61α (see (D)). The approximate position of the ER membrane is shown as a gray rectangle. (**C**) Surface representation of Sec63 and Sec71-72 with surface electrostatic potential shown. To show the positively charged surface of the Sec71-72 binding site on Sec63, Sec71-72 was intentionally separated from its original position in the Sec complex. Direction of association is indicated by an arrow. (**D** and **E**) Interactions of the Sec71 helix-tern-helix motif with Sec61α (**D**) and Sec63 (**E**).

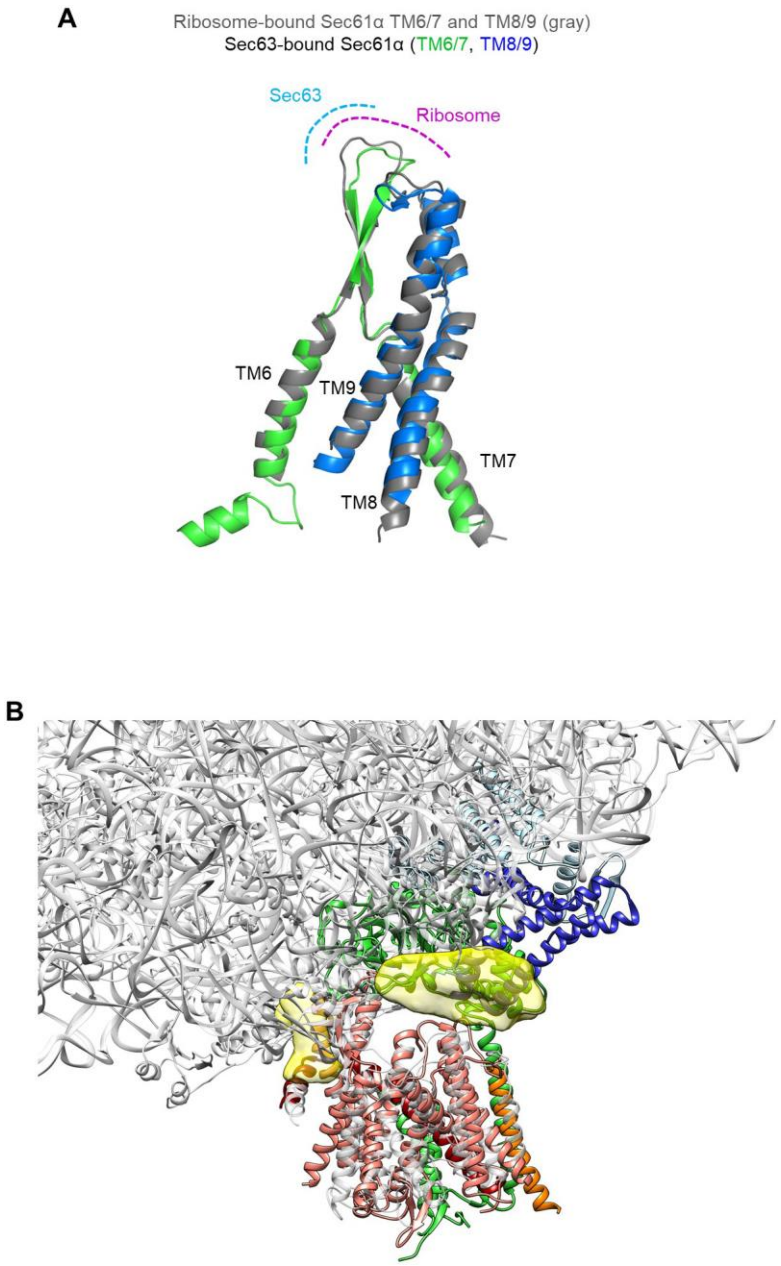

Fig. S5. Comparison between Sec61 binding to Sec63 and to a ribosome.

(**A**) Superimposition of TMs 6-9 of Sec61α between the yeast Sec complex (TM6/7 in green and TM8/9 in blue) and the *Sus scrofa* ribosome-bound Sec61 channel structures (gray; PDB ID: 3J7Q) (*14*). The binding site for Sec63 or the ribosome in L6/7 is indicated by cyan dashed line. (**B**) Superimposition between the yeast Sec complex (colored) and *Sus scrofa* ribosome-Sec61 complex (semitransparent gray). Sec62 is shown as semitransparent yellow density features.

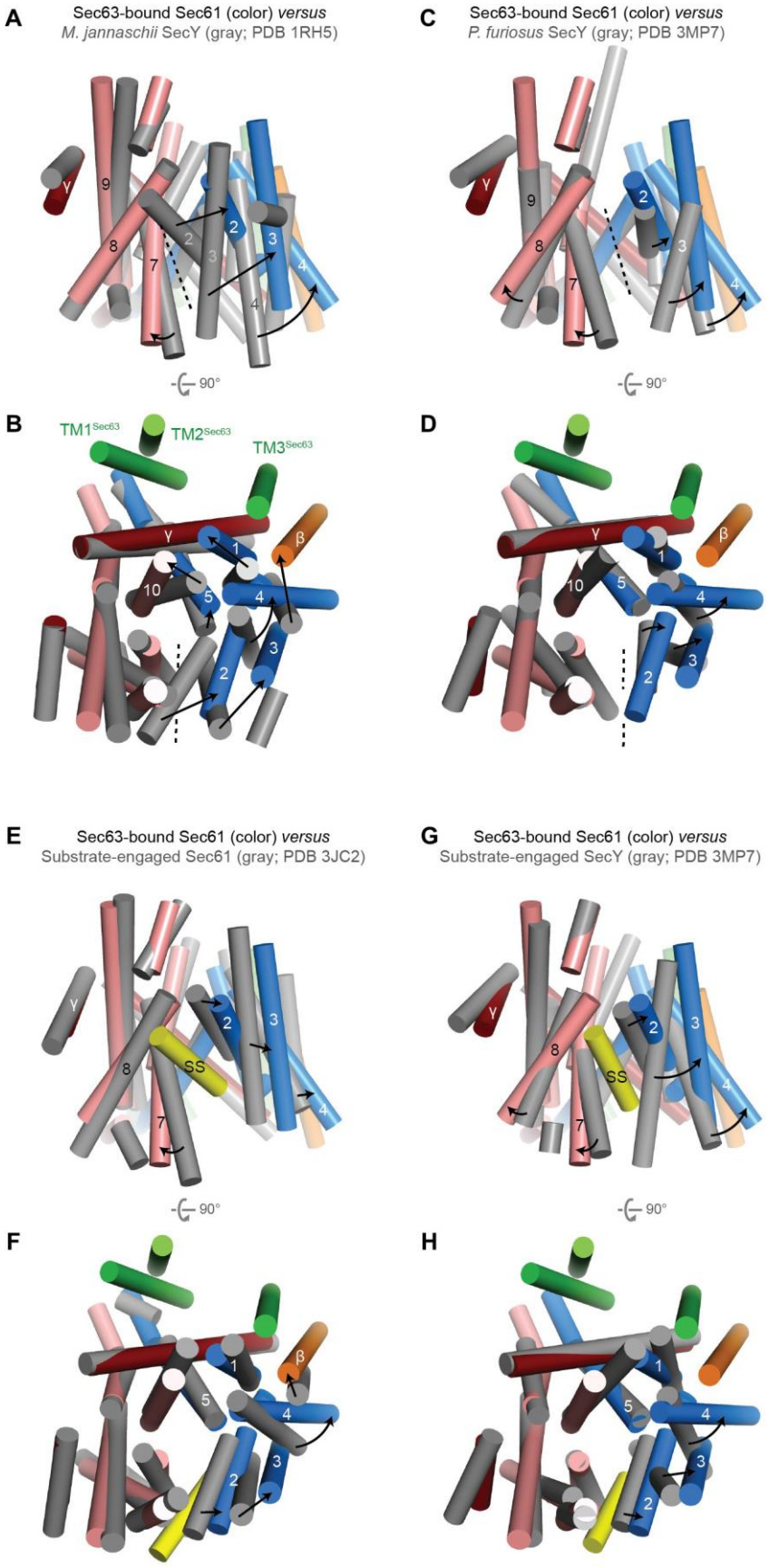
A
Sec63-bound Sec61 (color) versus
M. jannaschii SecY (gray; PDB 1RH5)
C
Sec63-bound Sec61 (color) versus
P. furiosus SecY (gray; PDB 3MP7)
90°
90°
B
TM1Sec63
TM2Sec63
TM3Sec63
D
E
Sec63-bound Sec61 (color) versus
Substrate-engaged Sec61 (gray; PDB 3JC2)
G
Sec63-bound Sec61 (color) versus
Substrate-engaged SecY (gray; PDB 3MP7)
SS
SS
90°
90°
F
H

Fig. S6. Opened lateral gate of Sec61 in the Sec complex.

(**A**–**D**) As in Fig. 3C–F, but the Sec61 channel was compared with the 'closed' *Methanocaldococcus jannaschii* SecY channel structure (PDB ID: 1RH5) (*4*) (A and B) or the 'open' *Pyrococcus furiosus* SecY channel structure (PDB ID: 3MP7) (*22*) (C and D). Shown are front (A and C; view into the lateral gate) and top (B and D; view from the cytosol) views. The N- and C- terminal halves of yeast Sec61α are shown in blue and salmon. To show a relative movement between the two halves, the structures are aligned with respect to the C-terminal half. Sec61β and Sec61γ are shown in orange and red, respectively. *M. jannaschii* and *P. furiosus* SecY channels are in gray. Numbers indicate corresponding TMs. In (B) and (D), the TMs of Sec63 are also shown (green). Dashed line, lateral gate. Note that *P. furiosus* SecY was crystallized in an open state. Although the mechanism of this opening is unclear, it has been suggested that this occurred by interactions between the TM10s of two neighboring SecY molecules in a crystal contact (*22*). Also note that yeast Sec61 is significantly more open than *P. furiosus* SecY. (**E**–**H**) As in (A–D), but the channel was compared with the ribosome-bound, substrate-engaged *Canis lupus* Sec61 channel (PDB ID: 3JC2) (*23*) (E and F) or the SecA-bound, substrate-engaged *Geobacillus thermodenitrificans* SecY channel (PDB ID: 5EUL) (*24*) (G and H). The signal sequence helices (SS) are shown in yellow. Note that in both structures, the signal sequences are located outside of the partially open lateral gate, exposed to the lipid phase, and thus the structures represent a 'post-insertion' state.

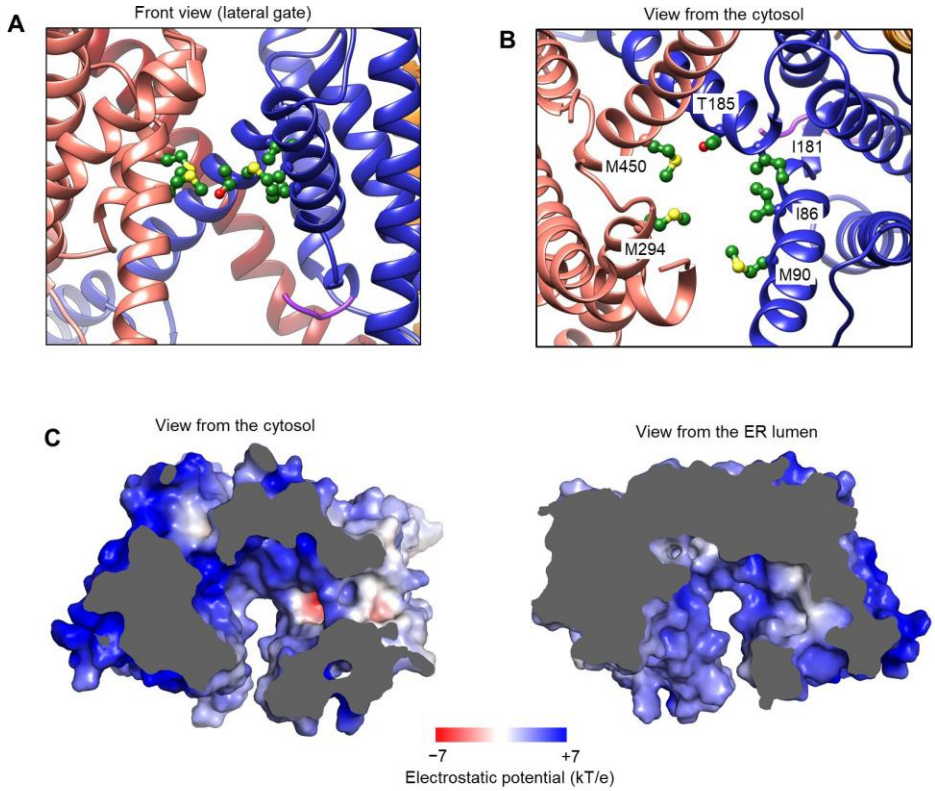

D

Position of pore-lining residues (numbering by *S. cerevisiae* Sec61α)

	Species	82	86	90	181	185	294	450
Fungi	*Saccharomyces cerevisiae*	Val	Ile	**Met**	Ile	**Thr**	**Met**	**Met**
	Schizosaccharomyces pombe	Ile	Val	**Met**	Ile	Ile	**Met**	Leu
	Candida albicans	Ile	Val	**Met**	Val	**Thr**	**Met**	Leu
	Komagataella pastoris	Ile	Val	**Met**	Ile	**Met**	**Met**	Leu
Protists	*Dictyostelium discoideum*	Ile	Val	**Met**	Ile	Ile	Ile	Leu
	Tetrahymena thermophila	Ile	Val	**Met**	Ile	Ile	Ile	Leu
	Salpingoeca rosetta	Ile	Val	**Met**	Ile	Ile	Ile	Leu
Metazoans	*Caenorhabditis elegans*	Ile	Val	Leu	Ile	Ile	Ile	Leu
	Drosophila melanogaster	Ile	Val	Leu	Ile	Ile	Ile	Leu
	Danio rerio	Ile	Val	Leu	Ile	Ile	Ile	Leu
	Homo sapiens	Ile	Val	Leu	Ile	Ile	Ile	Leu
Archaea	*Methanocaldococcus jannaschii*	Ile	Val	Ile	Ile	Ile	Ile	Leu
	Pyrococcus furiosus	Ile	Val	Ile	Ile	Ile	Ile	Leu
Bacteria	*Escherichia coli*	Ile	Ile	Ile	Ile	Ile	Ile	Ile
	Thermus thermophilus	Ile	Ile	Ile	**Thr**	Ile	Ile	Ile
	Geobacillus thermodenitrificans	Val	Ile	Ile	Ile	Ile	Ile	Ile

Fig. S7. Opened translocation pore of Sec61 in the Sec complex.

(**A** and **B**) Magnified views into the pore constriction (termed ‘pore ring’) of yeast Sec61α. (**C**) Surface electrostatic potential of Sec61’s cytosolic (left panel) and ER luminal (right panel) funnels. (**D**) Comparison of the Sec61α/SecY pore ring amino acids from various species. Non-aliphatic amino acids are in bold. Note that the original pore ring amino acids based on the *M. jannaschii* SecY structure (PDB: 1RH5) (*4*) does not include position 90. In the yeast Sec complex, position 90 seems to contribute to pore lining, whereas position 82 seems to contribute less.

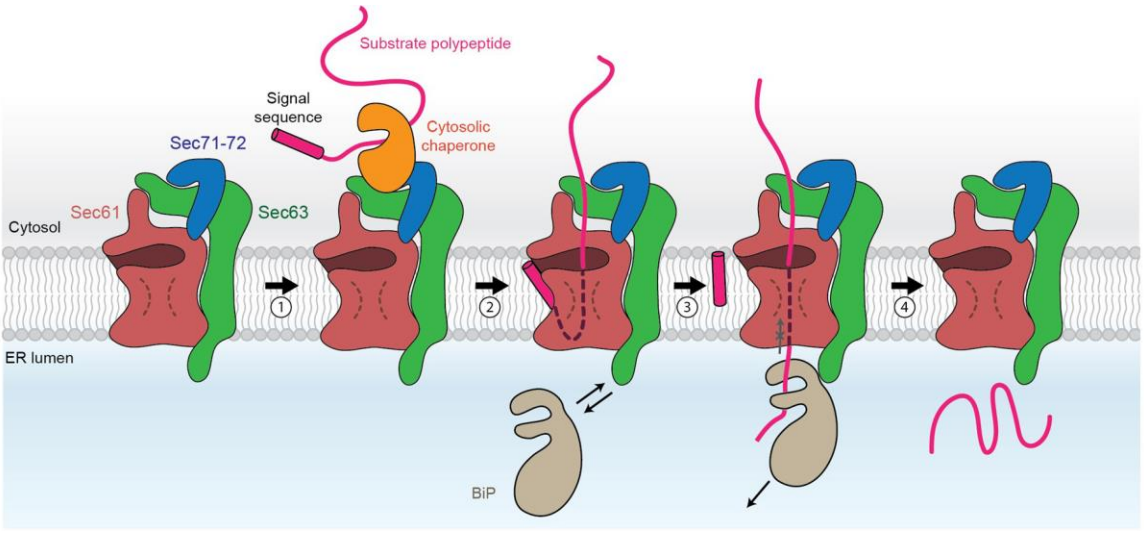

Fig. S8. Model for eukaryotic posttranslational protein translocation.

Step 1: a substrate bound to cytosolic Hsp70 or other chaperones is delivered to the Sec complex just above the channel by interaction with Sec72. In nonfungal species lacking Sec71-72, these factors may directly interact with Sec63 or Sec62 (not shown). Step2: the substrate inserts into the channel as a loop with the signal sequence helix exiting to the lipid phase through the lateral gate and the hydrophilic segment passing the pore. Upon substrate insertion, the lateral gate might close to some degree like the conformations seen in substrate-engaged ribosome-Sec61 and SecA-SecY complexes (not shown) (*23, 24*). Step 3: as the substrate emerges in the ER lumen, it is captured by BiP, which is posed just below the channel by the J-domain of Sec63. Multiple BiP molecules might bind to the substrate as translocation continues. Step 4: completion of translocation. Note that somewhere between steps 2 and 4, the signal sequence is cleaved by the signal peptidase.

Table S1. Cryo-EM image process and model statistics.

Cryo-EM data acquisition and single-particle analysis	
Data acquisition	
Microscope	FEI Talos Arctica
Acceleration voltage	200 kV
Camera (recording mode)	Gatan K2 Summit (super-resolution mode)
Magnification	43,103x
Pixel size	1.16 Å (super-resolution pixel size: 0.58 Å)
Electron dose rate and frame rate	1.25 e^- per $Å^2$ per frame; 0.2 s per frame
Total electron dose	50 e^- per $Å^2$
Defocus range	−0.8 μm to −2.4 μm
Number of micrographs collected	2,426
Number of micrographs used	2,162
Image processing and reconstruction	
Number of extracted particles	358,961 (box size: 256 pixels)
Number of particles after 2D classification	208,049
Number of particles used in reconstruction	172,531
Symmetry used for reconstruction	C1
Resolution, unmasked	6.98 Å (0.5 FSC); 4.39 Å (0.143 FSC)
Resolution, masked (corrected)	3.98 Å (0.5 FSC); 3.68 Å (0.143 FSC)
Range of resolutions contained in reconstruction (excluding highest and lowest 5%)	3.42 Å to 9.18 Å
Access code	
Density map (EM Databank)	EMD-0336
Atomic model (PDB)	6N3Q
Model Refinement (Phenix)	
Map pixel size (Å)	1.16
Map sharpening B-factor ($Å^2$)	-104.7
Map lowpass filter (Å)	3.68
Refinement resolution limit (Å)	3.70
Number of atoms	9,931
Protein	9,931
Non-protein	0
Model-to-map fit (Cross-correlation)	
Before refinement	0.764
After refinement	0.796
Refined Model Statistics	
Average B-factor ($Å^2$)	97.8
r.m.s deviations	
Bond length (Å)	0.006
Bond angle (°)	0.972
Ramachandran Plot	
Favored (%)	96.84
Outliers (%)	0.00
MolProbity	
Clash score* / percentile	4.48 (95 %)
Rotamers	
Favored (%)	93.86 %
Outliers (%)	0.67 %
Overall score /percentile	1.42 (97 %)
EMRiger Score	2.22

* number of steric overlaps > 0.4 Å per 1000 atoms